

**A measurement of  $Wb\bar{b}$  production and a search for monophoton signals of dark matter  
using the CMS detector at the CERN LHC**

by

Thomas Mastrianni Perry

A dissertation submitted in partial fulfillment of  
the requirements for the degree of

Doctor of Philosophy

(Physics)

at the

UNIVERSITY OF WISCONSIN-MADISON

2016

Date of final oral examination: 3 August 2016

The dissertation is approved by the following members of the Final Oral Committee:

Wesley Smith (Advisor), Professor, Physics

Sridhara Dasu, Professor, Physics

Matt Herndon, Professor, Physics

Yang Bai, Professor, Physics

David C. Schwartz, Professor, Chemistry

# CONTENTS

---

|  | Page       |
|--|------------|
| <b>List of Tables</b>  | <b>iii</b> |
| <b>List of Figures</b>   | <b>iv</b>  |
| <b>1 Quantum Field Theory and the Standard Model</b>   | <b>1</b>   |
| 1.1 Local Quantum Field Theory . . . . .   | 2          |
| 1.1.1 Representations of $SU(2)$ . . . . .   | 2          |
| 1.1.2 Yang-Mills Theory . . . . .  | 5          |
| 1.2 The Standard Model . . . . .   | 8          |
| 1.2.1 Gauge symmetry in $SU(3) \times SU(2) \times U(1)$ . . . . .                               | 8          |
| 1.2.2 Symmetry breaking in $SU(2) \times U(1) \rightarrow U(1)$ . . . . .                        | 10         |
| 1.2.3 Yukawa couplings and the CKM matrix . . . . .  | 12         |
| 1.3 Interpreting the Standard Model . . . . .  | 15         |
| 1.3.1 Scattering amplitude and propagators . . . . .   | 15         |
| 1.3.2 Path integrals and Feynman diagrams . . . . .  | 16         |
| 1.3.3 Renormalization . . . . .  | 18         |
| 1.3.4 Cross sections and decay rates . . . . .   | 20         |
| 1.3.5 QCD and Proton Structure . . . . .   | 23         |
| 1.4 Dark Matter . . . . .  | 25         |
| 1.4.1 Experimental motivations . . . . .   | 25         |
| 1.4.2 Simplified theoretical models . . . . .  | 26         |
| <b>2 Phenomenology of Processes</b>  | <b>27</b>  |
| 2.1 The Standard Model process $pp \rightarrow Wb\bar{b} \rightarrow \ell\nu b\bar{b}$ . . . . . | 27         |
| 2.1.1 $pp \rightarrow W$ . . . . .   | 27         |
| 2.1.2 $W \rightarrow \ell\nu$ . . . . .  | 28         |
| 2.1.3 $g \rightarrow b\bar{b}$ . . . . .   | 28         |
| 2.2 The Standard Model process $pp \rightarrow Z\gamma \rightarrow \nu\bar{\nu}\gamma$ . . . . . | 29         |

|          |  |           |
|----------|--|-----------|
| 2.2.1    | $pp \rightarrow Z/\gamma$  | 29        |
| 2.2.2    | $Z \rightarrow \nu\bar{\nu}$                                     | 30        |
| 2.2.3    | $pp \rightarrow Z\gamma$   | 30        |
| 2.3      | Dark matter models of $pp \rightarrow \gamma + \text{invisible}$ | 31        |
| <b>3</b> | <b>The LHC and CMS</b>   | <b>33</b> |
| 3.1      | The Large Hadron Collider  | 33        |
| 3.1.1    | <i>LHC pre-acceleration</i>                                      | 34        |
| 3.1.2    | <i>LHC acceleration</i>  | 34        |
| 3.2      | The Compact Muon Solenoid Detector                               | 37        |
| 3.2.1    | <i>Geometry</i>  | 39        |
| 3.2.2    | <i>Magnet</i>  | 40        |
| 3.2.3    | <i>Tracking System</i>   | 41        |
| 3.2.4    | <i>Electronic Calorimeter</i>                                    | 42        |
| 3.2.5    | <i>Hadronic Calorimeter</i>                                      | 43        |
| 3.2.6    | <i>Muon System</i>   | 45        |

## LIST OF TABLES

---

|     |   |    |
|-----|---|----|
| 1.1 | Representations of $SU(2) \times SU(2)$       | 3  |
| 1.2 | Standard Model quarks and leptons             | 9  |
| 1.3 | Covariant derivatives and fermion couplings   | 9  |
| 1.4 | Fundamental particle decay channels and rates | 23 |

## LIST OF FIGURES

---

|     |  |    |
|-----|--|----|
| 1.1 | Illustrations of SM couplings . . . . .  | 19 |
| 1.2 | Feynman diagrams for $2 \rightarrow 2$ scattering . . . . .                            | 19 |
| 1.3 | One-loop corrections to vertices and propagator . . . . .                              | 20 |
| 2.1 | Feynman diagrams for $pp \rightarrow Wb\bar{b} \rightarrow \ell\nu b\bar{b}$ . . . . . | 27 |
| 2.2 | Feynman diagrams for $pp \rightarrow Z\gamma \rightarrow \nu\bar{\nu}\gamma$ . . . . . | 29 |
| 2.3 | Feynman diagrams for dark matter monophoton . . . . .                                  | 32 |
| 3.1 | The LCH accelerator complex at CERN . . . . .  | 35 |
| 3.2 | The LHC dipole . . . . .   | 36 |
| 3.3 | The CMS Detector . . . . .   | 39 |
| 3.4 | The CMS Tracking System . . . . .  | 42 |
| 3.5 | The CMS Electromagnetic Calorimeter . . . . .  | 44 |
| 3.6 | The CMS Hadronic Calorimeter . . . . .   | 46 |
| 3.7 | The CMS Muon System . . . . .  | 48 |

# 1 QUANTUM FIELD THEORY AND THE STANDARD MODEL

---

The Standard Model of particle physics (SM) is useful. It is a local Quantum Field Theory (QFT) representing the forefront of contemporary understanding of nature on its finest level and is simultaneously the most quantitatively verified physical model of the constituent elements of the universe and known to be an incomplete description. It is therefore one of the goals of modern society to experimentally investigate particles and the interactions between particles within the context of the SM to validate the theory where possible and to guide directions for its extension where necessary. To achieve this goal, the governments from nearly 100 different countries, states and territories have funded tens of thousands of scientists, engineers and technicians to build, operate, maintain and analyze data from the Large Hadron Collider (LHC) at the European Center for Nuclear Research (CERN). This thesis presents analyses of data taken with the Compact Muon Solenoid (CMS) detector using proton-proton collisions provided by the LHC during its operation in 2012 and 2015.

## 1.1 Local Quantum Field Theory

### 1.1.1 Representations of $SU(2)$

One of the key underlying principles behind any QFT is that of symmetry. In particular, QFTs arise from the combination of quantum mechanics with Lorentz symmetry which ensures that the equations used to describe the laws of physics remain equivalently valid in all inertial reference frames. Local fields are therefore required to transform as representations of the Lorentz group, namely rotations,  $J_a$ , and boosts,  $K_a$  where  $a \in \{1, 2, 3\}$  for the three spatial dimensions. Boosts transform as vectors under rotation and the two obey the Lie algebras given in Equation 1.1, where  $\epsilon_{abc}$  is the Levi-Civita symbol.

$$[J_a, J_b] = i\epsilon_{abc}J_c, \quad [K_a, K_b] = -i\epsilon_{abc}J_c, \quad [J_a, K_b] = i\epsilon_{abc}K_c . \quad (1.1)$$

Both  $J_a$  and  $K_a$  are hermitian, but it is natural to define the non-hermitian objects

$$L_a = \frac{1}{\sqrt{2}}(J_a + iK_a), \quad R_a = \frac{1}{\sqrt{2}}(J_a - iK_a) \quad (1.2)$$

which commute with each other and each independently obey the commutation relations of  $SU(2)$ ,

$$[L_a, L_b] = i\epsilon_{abc}L_c, \quad [R_a, R_b] = i\epsilon_{abc}R_c, \quad [L_a, R_b] = 0 . \quad (1.3)$$

**Table 1.1:** Selected representations of the Lorentz group are formed by combining representations of  $SU(2)$  in the structure  $SU(2)_L \times SU(2)_R$ . The first column labels the quantum numbers,  $\lambda$ , and the second column translates this into dimensionality. The third column indicates the kind of object which meets the symmetry requirements.

| $(\lambda_L, \lambda_R)$ | $(d_L, d_R)$ | Name     |                          |
|--------------------------|--------------|----------|--------------------------|
| $(0, 0)$                 | $(1, 1)$     | $\phi$   | Scalar                   |
| $(1/2, 0)$               | $(2, 1)$     | $\psi_L$ | Left-handed Weyl spinor  |
| $(0, 1/2)$               | $(1, 2)$     | $\psi_R$ | Right-handed Weyl spinor |
| $(1/2, 1/2)$             | $(2, 2)$     | $A_\mu$  | Gauge potential          |

Because of this, the Lorentz group may be expressed in terms of representations of  $SU(2)_L \times SU(2)_R$ .

The group  $SU(2)$  can be thought of as the set of  $2 \times 2$  complex matrices with unit determinant under the operation of matrix multiplication, and the  $(2^2 - 1)$  generators of the group are proportional to the Pauli matrices,

$$\sigma_1 = \begin{pmatrix} 0 & 1 \\ 1 & 0 \end{pmatrix}, \quad \sigma_2 = \begin{pmatrix} 0 & -i \\ i & 0 \end{pmatrix}, \quad \sigma_3 = \begin{pmatrix} 1 & 0 \\ 0 & -1 \end{pmatrix} \quad (1.4)$$

which have been diagonalized along the 3 direction and combine with the unit matrix to form  $\sigma^\mu = (\mathbf{1}, \vec{\sigma})$ . Representations of  $SU(2)$  are labelled by a quantum number,  $\lambda \in \{0, 1/2, 1, 3/2, \dots\}$ , with the fundamental representation being  $\lambda = 1/2$  and the dimensionality,  $d$ , of a representation being set by  $d = 2\lambda + 1$ . Representations of the full symmetry are therefore constructed by combining representations from the  $L$  and  $R$  components, and Table 1.1 illustrates those combinations of lowest dimensionality.

Rotations take spatial coordinates into spatial coordinates, but boosts mix spatial

coordinates with time, which have opposite signs in the spacetime metric. Therefore, under the parity operation,  $P$ , which inverts the signs of spatial coordinates,

$$P : J \rightarrow J, \quad P : K \rightarrow -K , \quad (1.5)$$

while, under conjugation,  $C$ , because  $J$  and  $K$  are hermitian,

$$C : J \rightarrow J, \quad C : K \rightarrow K . \quad (1.6)$$

Using Equation 1.2 then, the  $(\frac{1}{2}, 0)$  and  $(0, \frac{1}{2})$  representations transform as

$$P : \psi_{L(R)} \rightarrow \psi_{R(L)}, \quad C : \psi_{L(R)} \rightarrow \sigma_2 \psi_{R(L)}^*, \quad CP : \psi_{L(R)} \rightarrow \sigma_2 \psi_{L(R)}^* . \quad (1.7)$$

which illustrates the point that because  $\psi_L$  and  $\psi_R$  can be interchanged via these discrete transformations, they are not independent. The full  $SU(2)_L \times SU(2)_R$  symmetry can thus be maintained by considering only one of the two, and it is customary to work with  $\psi_L$ , the ‘left’ component, henceforth simply denoted as  $\psi$ , with  $\sigma_2 \psi_R^*$  denoted as  $\bar{\psi}$ . An object which transforms as a vector can be made from spinors by noting<sup>1</sup> that  $(\frac{1}{2}, 0) \times (0, \frac{1}{2}) = (\frac{1}{2}, \frac{1}{2})$ . Therefore  $\psi^\dagger \sigma^\mu \psi$  transforms as a Lorentz vector, and can be used to make a Lorentz-invariant object by contracting the spacetime index,  $\mu$ . The derivative operator  $\partial_\mu = (\partial/\partial t, \partial/\partial \vec{x})$  is translation-invariant and does not give a surface contribution if inserted between the two instances of  $\psi$ ,

---

<sup>1</sup> $d = 2 \times 2(\frac{1}{2}) + 1 = 4$  for  $(t, x, y, z)$

motivating the canonical kinetic term for spinors,

$$i\psi^\dagger \sigma^\mu \partial_\mu \psi . \quad (1.8)$$

### 1.1.2 Yang-Mills Theory

The above construction for canonical kinetic terms in the Lagrangian was generalized by Chen Ning Yang and Robert Mills for  $N$  spinor fields as

$$i \sum_{a=1}^N \psi^{a\dagger} \sigma^\mu \partial_\mu \psi_a = i\Psi^\dagger \sigma^\mu \partial_\mu \Psi , \quad (1.9)$$

and while the existence of this object is imposed by the Lorentz symmetry, further symmetries can be made apparent. A simple example is global phase invariance. For  $\lambda$  which is not a function of  $x$ , the transformation  $\Psi \rightarrow e^{i\lambda} \Psi$  leaves the kinetic term in Equation 1.9 unchanged. The derivative passes through  $e^{i\lambda}$  which combines with  $e^{-i\lambda}$  from the transform on  $\Psi^\dagger$  to make the unit.

A more complicated example is gauge invariance. The symmetry of global phase invariance can be extended by introducing  $(N^2 - 1)$  traceless hermitian matrices,  $\lambda_A$  which satisfy the Lie algebra,

$$[\lambda_A, \lambda_B] = if_{ABC}\lambda_C, \quad \text{Tr}(\lambda_A \lambda_B) = \frac{1}{2}\delta_{AB} , \quad (1.10)$$

where  $f_{ABC}$  are the structure functions for  $SU(N)$  and  $\delta_{AB}$  is the Kronecker delta function. For  $N = 2$ ,  $f_{ABC} = \epsilon_{abc}$  used in Equations 1.1 and  $\lambda_A$  are the Pauli matrices from Equations 1.4. For  $N = 3$ ,  $f_{ABC}$  is also a totally anti-symmetric operator and

$\lambda_A$  are the Gell-Mann matrices.

These  $\lambda_A$  can each be used to construct a hermitian ( $N \times N$ ) matrix. One degree of freedom is factored out as the overall phase of the trace, demonstrated to be a symmetry of  $\Psi$ . This leaves  $(N - 1)$  degrees from the real diagonal elements and  $2 \times (N^2 - N)/2$  from the unique complex off-diagonal elements. These  $(N^2 - 1)$  overall degrees of freedom correspond to the  $\lambda_A$  which are used to construct

$$\mathbf{H} = \frac{1}{2} \sum_{A=1}^{N^2-1} \omega_A \lambda_A \quad (1.11)$$

using  $\omega_A$  as the parameter of expansion.

$\mathbf{H}$  can then be used to produce a unitary matrix

$$\mathbf{U} = e^{i\mathbf{H}} \quad (1.12)$$

whose unitarity is evident by the hermiticity of  $\mathbf{H}$ . Unitarity is crucial for the final cancellation to leave Equation 1.9 invariant under the gauge transformation  $\Psi \rightarrow \mathbf{U}\Psi$ , but to ensure locality, the particular expansion,  $\omega_a$ , could have dependence on position and thus interact with  $\partial_\mu$ .

To accommodate for this, the derivative is generalized into an ( $N \times N$ ) covariant derivative matrix,  $\mathbf{D}_\mu$ , which has the property

$$\mathbf{D}'_\mu \mathbf{U} \Psi = \mathbf{U} \mathbf{D}_\mu \Psi \quad (1.13)$$

and thus behaves under gauge transformations as

$$\Psi \rightarrow \mathbf{U}\Psi, \quad \mathbf{D}_\mu \rightarrow \mathbf{D}'_\mu = \mathbf{U}\mathbf{D}_\mu\mathbf{U}^\dagger \quad . \quad (1.14)$$

Explicitly,  $\mathbf{D}_\mu$  is constructed using  $(N^2 - 1)$  gauge potentials,  $A_\mu$ , in the form of a hermitian matrix,

$$\mathbf{A}_\mu = \frac{1}{2} \sum_{B=1}^{N^2-1} A_\mu^B \boldsymbol{\lambda}_B \quad (1.15)$$

which transforms under gauge transformations as

$$\mathbf{A}_\mu \rightarrow \mathbf{A}'_\mu = -i\mathbf{U}\partial_\mu\mathbf{U}^\dagger - i\mathbf{U}\mathbf{A}_\mu\mathbf{U}^\dagger \quad . \quad (1.16)$$

The field strength matrix is formed by taking the commutator

$$\mathbf{F}_{\mu\nu} = -i[\mathbf{D}_\mu, \mathbf{D}_\nu] \quad (1.17)$$

which leads to a kinetic term that is invariant under both gauge and Lorentz transformations,  $-1/2g^2\text{Tr}(\mathbf{F}_{\mu\nu}\mathbf{F}^{\mu\nu})$  where  $g$  is the coupling strength. This leads to the Yang-Mills Lagrange density of

$$\mathcal{L}_{\text{YM}} = -\frac{1}{2}\text{Tr}(\mathbf{F}_{\mu\nu}\mathbf{F}^{\mu\nu}) + i\Psi^\dagger\sigma^\mu\mathbf{D}_\mu\Psi + i\bar{\Psi}^\dagger\sigma^\mu\overline{\mathbf{D}}_\mu\bar{\Psi} \quad . \quad (1.18)$$

For  $N = 2$ , this is the Quantum ElectroDynamics (QED) Lagrangian of electromagnetic interactions with a massless electron, and for  $N = 3$ , this is Quantum ChromoDynamics (QCD).

## 1.2 The Standard Model

### 1.2.1 Gauge symmetry in $SU(3) \times SU(2) \times U(1)$

The Standard Model (SM) Lagrangian uses the Yang-Mills construction on the group  $SU(3) \times SU(2) \times U(1)$ . Strong interactions are described by  $SU(3)$  (color) which has eight gluons,  $G_\mu^A$ ,  $A \in 1, 2, \dots, 8$ . Electroweak interactions incorporate the mixing of  $SU(2) \times U(1)$  via the Higgs mechanism with  $SU(2)$  (weak charge) having three weak bosons,  $W_\mu^a$ ,  $a \in 1, 2, 3$  and  $U(1)$  (hypercharge) having one hyperon  $B_\mu$ . The field strengths are independent, with independent coupling constants  $g_3, g_2, g_1$ , each calculated using the appropriate covariant derivative in Equation 1.17. This is part of the SM Lagrangian describing the gauge bosons,

$$\mathcal{L}_{\text{bosons}} = -\frac{1}{4g_3^2}G_{\mu\nu}^AG^{\mu\nu A} - \frac{1}{4g_2^2}W_{\mu\nu}^aW^{\mu\nu a} - \frac{1}{4g_1^2}B_{\mu\nu}B^{\mu\nu} . \quad (1.19)$$

The matter (antimatter) components are the spin-1/2 fermions which are built from the  $L$  representation of Weyl spinors and are listed in Table 1.2. The portion of the SM Lagrangian coming from the fermion kinetic terms is found by exchanging the derivative for the appropriate covariant derivative in Equation 1.9 to be

$$\mathcal{L}_{\text{fermions}} = i \sum_{i=1}^3 \left( \mathbf{Q}_i^\dagger \sigma^\mu \mathbf{D}_\mu \mathbf{Q}_i + L_i^\dagger \sigma^\mu \mathbf{D}_\mu L_i + \bar{\mathbf{u}}_i^\dagger \sigma^\mu \mathbf{D}_\mu \bar{\mathbf{u}}_i + \bar{\mathbf{d}}_i^\dagger \sigma^\mu \mathbf{D}_\mu \bar{\mathbf{d}}_i \bar{e}_i^\dagger \sigma^\mu \mathbf{D}_\mu \bar{e}_i \right) \quad (1.20)$$

with the covariant derivatives described in Table 1.3.

Both quarks and leptons come in three families, known as generations for the quarks and flavors for the leptons. The leptons are colorless and therefore do not

**Table 1.2:** Fermions in the standard model consist of three families ( $i \in 1, 2, 3$ ) of leptons and quarks in the singlet and doublet configurations. The symmetries are noted as  $(SU(3)^c, SU(2))_Y$  where  $Y$  is chosen to satisfy the Gell-Mann-Nishijima formula, Equation 1.21.

| Name           | Symbol  | $I_3$                                       | Symmetry          |
|----------------|---|---|-------------------|
| Quark doublet  | $\mathbf{Q}_i = \begin{pmatrix} u_i \\ d_i \end{pmatrix}$ | $\begin{pmatrix} 1/2 \\ -1/2 \end{pmatrix}$ | $(3^c, 2)_{1/3}$  |
| Lepton doublet | $L_i = \begin{pmatrix} \nu_i \\ e_i \end{pmatrix}$        | $\begin{pmatrix} 1/2 \\ -1/2 \end{pmatrix}$ | $(1^c, 2)_{-1}$   |
| Quark singlet  | $\bar{\mathbf{u}}_i$                                      | 0   | $(3^c, 1)_{-4/3}$ |
| Quark singlet  | $\bar{\mathbf{d}}_i$                                      | 0   | $(3^c, 1)_{2/3}$  |
| Lepton singlet | $\bar{e}_i$   | 0   | $(1^c, 2)_2$      |

**Table 1.3:** The exact form of the covariant derivative used is determined by the couplings to gauge bosons the fermion has. Below, the fermions are listed, along with the associated derivative and interactions. On the bottom are the vectors of gauge potentials as defined in Equation 1.15.

| Fermion type               | Covariant derivative  | Interactions |         |        |
|----------------------------|---|--------------|---------|--------|
|                            |   | $SU(3)$      | $SU(2)$ | $U(1)$ |
| All quarks (doublet)       | $\mathbf{D}_\mu \mathbf{Q}_i = \left( \partial_\mu + i\mathbf{G}_\mu + i\mathbf{W}_\mu + \frac{i}{3}B_\mu \right) \mathbf{Q}_i$ | Yes          | Yes     | Yes    |
| All leptons (doublet)      | $\mathbf{D}_\mu L_i = \left( \partial_\mu + i\mathbf{W}_\mu + \frac{i}{2}B_\mu \right) L_i$                                     | No           | Yes     | Yes    |
| $u$ -type quarks (singlet) | $\mathbf{D}_\mu \bar{\mathbf{u}}_i = \left( \partial_\mu - i\mathbf{G}_\mu^* - \frac{2i}{3}B_\mu \right) \bar{\mathbf{u}}_i$    | Yes          | No      | Yes    |
| $d$ -type quarks (singlet) | $\mathbf{D}_\mu \bar{\mathbf{d}}_i = \left( \partial_\mu - i\mathbf{G}_\mu^* + \frac{i}{3}B_\mu \right) \bar{\mathbf{d}}_i$     | Yes          | No      | Yes    |
| Charged leptons (singlet)  | $\mathbf{D}_\mu \bar{e}_i = \left( \partial_\mu + iB_\mu \right) \bar{e}_i$   | No           | No      | Yes    |

$\mathbf{G}_\mu = G_\mu^A \lambda^A / 2, \quad \mathbf{G}_\mu^* = G_\mu^A \lambda^{A*} / 2, \quad \mathbf{W}_\mu = W_\mu^a \sigma^a / 2$

couple to gluons, but the quarks do and additionally come in three color varieties for each generation. The singlet configurations contain only electrically charged fermions,

and all fermions have their charge set by the Gell-Mann-Nishijima formula,

$$Q = I_3 + \frac{Y}{2} \quad , \quad (1.21)$$

where  $I_3$  is the component of weak isospin,  $SU(2)$ , along the direction in which the Pauli matrices in Equations 1.4 are diagonalized.

All quarks and leptons can exist in  $SU(2)$  doublet configurations, and the different  $I_3$  values further break quarks and leptons into types. For quarks, there are  $u$ -type ( $u, c, t$ ) = (up, charm, top) which have charge  $+2/3$ , and there are  $d$ -type ( $d, s, b$ ) = (down, strange, bottom) which have charge  $-1/3$ . Leptons are either charged ( $e, \mu, \tau$ ) = (electron, muon, tauon) or neutral ( $\nu_e, \nu_\mu, \nu_\tau$ ) = (electron-, mu-, tau-neutrino), and all charged fermions are arranged such that mass increases with successive generations within a given type. In units where  $\hbar = c = 1$ , the top ( $m_t = 173$  GeV) and bottom ( $m_b = 4$  GeV) are the heaviest quarks of their respective types, with the bottom weighing three orders of magnitude greater than the lightest quark, up ( $m_u = 2$  MeV). The mass separation for the charged leptons ( $m_\tau = 1.7$  GeV,  $m_e = 0.5$  MeV) also spans multiple orders of magnitude, but while the observations of neutrino oscillations indicate that neutrinos have mass, only upper limits on the values they may have have been set on the order of MeV.

### 1.2.2 Symmetry breaking in $SU(2) \times U(1) \rightarrow U(1)$

Fermions and gauge bosons are massless as written in  $\mathcal{L}_{\text{fermions}}$  and  $\mathcal{L}_{\text{bosons}}$ , but are observed to be massive in nature and can acquire mass through the Brout-Englert-

Higgs mechanism. A scalar (spin-zero) field as given in the top row of Table 1.1 is introduced in a doublet configuration. This adds a Higgs term to the SM Lagrangian,

$$\mathcal{L}_{\text{Higgs}} = (\mathbf{D}_\mu H)^\dagger \mathbf{D}_\mu H + m_H H^\dagger H - \lambda (H^\dagger H)^2 , \quad (1.22)$$

where the first term is the canonical kinetic term for a scalar, the second term generates the mass of the Higgs boson ( $m_H$ ) and the third term is a potential. This is minimized when

$$H_0^\dagger H_0 = \frac{m^2}{2\lambda} = \frac{v^2}{2}, \quad H_0 = \frac{1}{\sqrt{2}} \begin{pmatrix} 0 \\ v \end{pmatrix} . \quad (1.23)$$

Taking perturbations about the minimum vacuum expectation value using the Kibble parameterization,  $v \rightarrow v + h(x)$  and the unitary matrix containing three Nambu-Goldstone bosons from the symmetry breaking is factored out, yielding

$$H = \frac{1}{\sqrt{2}} \mathbf{U}(x) \begin{pmatrix} 0 \\ v + h(x) \end{pmatrix} . \quad (1.24)$$

In this gauge, the weak bosons,  $W_{\mu\nu}^a$ , and the hyperion,  $B_\mu$  appear in Equation 1.25 as linear combinations as the massive  $W^\pm$  and  $Z$  bosons, and as the massless photon respectively,

$$\begin{aligned} W_\mu^\pm &= \frac{1}{\sqrt{2}} (W_\mu^1 \mp iW_\mu^2), & Z_\mu &= \cos \theta_W W_\mu^3 - \sin \theta_W B_\mu, & A_\mu &= \sin \theta_W W_\mu^3 + \cos \theta_W B_\mu \\ M_Z &= \frac{v}{2} \sqrt{g_1^2 + g_2^2}, & M_W &= \cos \theta_W M_Z \end{aligned} . \quad (1.25)$$

Here, the Weinberg angle,  $\theta_W = g_1/g_2$ , is the ratio between the  $U(1)$  and  $SU(2)$ . The  $\pm$  in  $W_\mu^\pm$  aligns with the electric charge of the  $W$  boson, and the  $Z_\mu$  and  $A_\mu$  are both electrically neutral and orthogonal.

The vector boson couplings to the fermions are then expressed as three types of currents. Electromagnetic interactions,  $J_\mu^\gamma$ , involve couplings between the photon,  $\gamma$ , and charged particles, and any particle which interacts with the photon can also interact with the  $Z$  boson. The neutral current interactions,  $J_\mu^Z$ , have additional couplings to the lepton and quark doublets and the charged current interactions,  $J_\mu^\pm$ , are between the doublets and the  $W$  bosons. Couplings to each of the bosons are scaled by a coupling factor which decides the relative strengths of the interactions, and the Lagrangian for the currents is given in Equation 1.26 where  $i$  indicates the generation.

$$\begin{aligned}
\mathcal{L}_{\text{currents}} &= eA^\mu J_\mu^\gamma + g_Z Z^\mu J_\mu^Z + g_W W^{+\mu} J_\mu^- + G_W W^{-\mu} J_\mu^+ \\
J_\mu^\gamma &= \bar{e}_i^\dagger \sigma_\mu e_i + e_i^\dagger \sigma_\mu e_i + \frac{2}{3} \mathbf{Q}_{i1}^\dagger \sigma_\mu \mathbf{Q}_{i1} - \frac{1}{3} \mathbf{Q}_{i2}^\dagger \sigma_\mu \mathbf{Q}_{i2} - \frac{2}{3} \bar{\mathbf{u}}_i^\dagger \sigma_\mu \bar{\mathbf{u}}_i + \frac{1}{3} \bar{\mathbf{d}}_i^\dagger \sigma_\mu \bar{\mathbf{d}}_i \\
J_\mu^Z &= L_i^\dagger \frac{\tau_3}{2} \sigma_\mu L_i + \mathbf{Q}_i^\dagger \frac{\tau_3}{2} \sigma_\mu \mathbf{Q}_i - \sin^2 \theta_W J_\mu^\gamma \\
J_\mu^\pm &= L_i^\dagger \tau_\pm \sigma_\mu L_i + \mathbf{Q}_i^\dagger \tau_\pm \sigma_\mu \mathbf{Q}_i \\
e &= \frac{g_1 g_2}{\sqrt{g_1^2 + g_2^2}}, \quad g_Z = \frac{e}{\cos \theta_W \sin \theta_W}, \quad g_W = \frac{e}{\sqrt{2} \sin \theta_W}
\end{aligned} \tag{1.26}$$

### 1.2.3 Yukawa couplings and the CKM matrix

In addition to generating mass terms for the bosons, the Higgs field gives rise to fermion mass via Yukawa couplings between the Higgs doublet,  $H$ , from Equation 1.22 and the fermion doublets. A singlet configuration is possible to construct from

two  $SU(2)$  doublets in their antisymmetric combination<sup>2</sup>, of the general form  $(MN)$  where  $M$  and  $N$  are both  $L$  fermion fields. Each term has an associated Yukawa coupling,  $\mathbf{Y}^f = y_{ij}$ , where  $f \in \{u, d, e\}$  for each of the charged fermion types, and this piece of the SM the Lagrangian is

$$\begin{aligned}\mathcal{L}_{\text{Yukakwa}} &= y_{ij}^u \mathbf{Q}_i \bar{\mathbf{u}}_j H + y_{ij}^d \mathbf{Q}_i \bar{\mathbf{d}}_j \bar{H} + y_{ij}^e L_i \bar{e}_j \bar{H} \\ &= \mathcal{L}_{\text{Yuk}}^u + \mathcal{L}_{\text{Yuk}}^d + \mathcal{L}_{\text{Yuk}}^e\end{aligned}. \quad (1.27)$$

In general, any  $(3 \times 3)$  matrix can written in terms of a diagonal matrix  $D$  and two unitary matrices  $U$  and  $V$ , and in particular, the coupling matrices can be expressed as  $\mathbf{Y}^f = \mathbf{U}^f \mathbf{D}^f \mathbf{V}^f$ . The fermion Yukawa couplings are all of the form  $\mathbf{Y}^f \mathbf{F} \bar{\mathbf{f}}$  and by incorporating  $\mathbf{V}^f$  into  $\bar{\mathbf{f}}$ , the may each be individually diagonalized as

$$\begin{aligned}\mathcal{L}_{\text{Yuk}}^e &= (m_e(\bar{e}e) + m_\mu(\bar{\mu}\mu) + m_\tau(\bar{\tau}\tau)) \beta(h) \\ \mathcal{L}_{\text{Yuk}}^d &= (m_d(\bar{d}d) + m_\mu(\bar{s}s) + m_\tau(\bar{b}b)) \beta(h) \\ \mathcal{L}_{\text{Yuk}}^u &= (m_u(\bar{u}u) + m_\mu(\bar{c}c) + m_\tau(\bar{t}t)) \beta(h)\end{aligned} \quad (1.28)$$

where  $\beta$  is a function of the Higgs coupling,  $h$ . The mass terms for the gauge bosons are also proportional to  $h$ . It is because the mass of the Higgs boson is tied to the masses of the gauge bosons and charged fermions that the discovery of the Higgs boson in 2012 was of such importance. The result was announced just a few months after I moved to Geneva to do research at CERN, and it provided the first measurement of a parameter in the SM that had been previously unknown,  $m_H = 125\text{GeV}$ .

Unlike the leptons, which contain only one charged type, the quarks have two

---

<sup>2</sup> The second term in  $(1/2, 0) \times (1/2, 0) = (1, 0) + (0, 0)$

different spinor fields, **u** and **d**, which are different but both have Yukawa couplings to the Higgs with the same **Q**. This means that while the lepton sector  $\mathcal{L}_{\text{Yuk}}^e$  can be diagonalized in mass simultaneously with either of  $\mathcal{L}_{\text{Yuk}}^d$  or  $\mathcal{L}_{\text{Yuk}}^u$ , the quarks can not be simultaneously diagonalized. The mismatch between the two types of quarks is characterized by the unitary Cabibbo-Kobayashi-Maskawa (CKM) matrix,

$$\mathcal{U}_{\text{CKM}} = \mathbf{U}^d \overline{\mathbf{U}}^{u\dagger} = \begin{pmatrix} c_1 & +s_1c_3 & +s_1s_3 \\ -s_1c_2 & c_1c_2c_3 - s_2s_3e^{i\delta} & c_1c_2s_3 + s_2c_3e^{i\delta} \\ -s_1s_2 & c_1s_2c_3 + c_2s_3e^{i\delta} & c_1s_2s_3 - c_2c_3e^{i\delta} \end{pmatrix} \quad (1.29)$$

where  $s_a$  and  $c_a$  stand for  $\sin \theta_a$  and  $\cos \theta_a$ . In this choice of basis, the charged current interactions from Equation 1.26 are

$$J_\mu^\pm = L_i^\dagger \tau_\pm \sigma_\mu L_i + \mathbf{d}_i^\dagger (\mathcal{U}_{\text{CKM}})_{ij} \tau_\pm \sigma_\mu \mathbf{u}_j \quad . \quad (1.30)$$

The CKM matrix thus is a matrix of coefficients for transforming between generations and types of quarks for charged current interactions. It also is the location in the SM where parity invariance is violated.

The laws of nature are postulated to be invariant under the combined operation  $CPT$ , where  $C$  and  $P$  are defined in Equations 1.5 and 1.6, and  $T$  is the antiunitary time-reversal operator,

$$T^{-1}iT = -i \quad (1.31)$$

Because of the complex phase,  $\delta$ , in the CKM matrix, the couplings between the quarks and  $W$  bosons are not  $T$  invariant. To maintain  $CPT$  invariance,  $\delta \neq 0$

implies that  $CP$  must be violated in such interactions.

## 1.3 Interpreting the Standard Model

### 1.3.1 Scattering amplitude and propagators

Initial and final states are built by successive applications of the raising (or particle creation) operator,  $a^\dagger$ , on the vacuum,  $|0\rangle$ , at the limit of initial states being measured infinitely far in the past and final states being measured infinitely far in the future.

$$|i\rangle = \lim_{t \rightarrow -\infty} \sum_i a_i^\dagger |0\rangle, \quad |f\rangle = \lim_{t \rightarrow +\infty} \sum_{i'} a_{i'}^\dagger |0\rangle \quad (1.32)$$

The overlap or scattering amplitude between these states,  $\langle f|i\rangle$ , can be expressed using the Lehmann-Symanzik-Zimmermann (LSZ) reduction formula in Equation 1.33 as factored into two pieces,

$$\langle f|i\rangle = i^{n_j+n_{j'}} \int \prod_j d^4x_j e^{ik_j x_j} (-\partial_j^2 + m^2) \times \langle 0|T \prod_j \phi(x_j)|0\rangle \quad (1.33)$$

The first piece is made of integrals over the momenta,  $k_j$  for  $j \in j, j'$ , of the  $n_j$  incoming and  $n_{j'}$  outgoing particles. In these integrals, each plane wave multiplies the function  $(-\partial_j^2 + m^2)$  where  $\partial_j^2 = \partial_j^\mu \partial_{\mu j}$  is the contraction of the Lorentz-invariant derivative operator. The second piece of the LSZ formula is the vacuum expectation value of the time-ordered product of fields,  $\langle 0|T \prod_j \phi(x_j)|0\rangle$ .

By Wick's theorem, the time-ordered interaction of  $n$  fields is identically zero for

odd numbers of fields, and for even numbers of fields is

$$\langle 0 | T\phi(x_1) \dots \phi(x_{2n}) | 0 \rangle = \frac{1}{i^n} \sum_{\text{pairs}} \Delta(x_{i1} - x_{i2}) \dots \Delta(x_{i_{2n-1}} - x_{i_{2n}}). \quad (1.34)$$

In this equivalence,  $\Delta(x - x')$  is the Feynman propagator between  $x$  and  $x'$  and is Green's function for the Klein-Gordan equation which contains the same  $(-\partial_j^2 + m^2)$  term as multiplies in the integrals,

$$(-\partial_x^2 + m^2) \Delta(x - x') = \delta^4(x - x') . \quad (1.35)$$

In this way the two components of the LSZ formulation interact. The integrals contain factors of  $(-\partial^2 + m^2)$  and the propagators contain factors of  $1/(-\partial^2 + m^2)$ . The on-shell requirement, that  $|f\rangle$  and  $|i\rangle$  have fixed masses causes  $(-\partial^2 + m^2) \rightarrow 0$ . This term in the integral cancels exactly with the corresponding diverging term in the appropriate propagator, but sets to zero the terms which do not have this divergence. This is the mechanism by which final state particles are observed to be on their mass shell, or on-shell, while allowing for interactions to happen between particles at varying masses, off-shell, with varying probabilities.

### 1.3.2 Path integrals and Feynman diagrams

To calculate the expression in 1.34, an integral over paths through the space of field configurations is used. This is called the path integral,  $Z(J)$ , and is a function of the

Lagrangian,  $\mathcal{L}$ , current sources,  $J$ , and fields,  $\phi$ ,

$$Z(J) = \langle 0|0 \rangle_J = \int \mathcal{D}\phi e^{i \int d^4x (\mathcal{L} + J\phi)} . \quad (1.36)$$

The fundamental interactions between particles as described by  $Z(J)$  can be visually represented using the Feynman diagram notation. On a 2-D spacetime plane,  $(x, t)$ , lines representing particles meet at a vertex, which is the interaction point. Fermions are represented using solid lines with an arrow indicating a direction. If the component of the arrow in the  $t$  dimension is positive, the particle fermion is indicated, and if it is negative, the antiparticle is meant. In this way, by rotating  $(x, t) \rightarrow (x', t')$  a single diagram can be interpreted as depicting possibly more than one interaction.

To describe the scattering of fermions and gauge bosons in the SM, diagrams with the appropriate initial and final state particles are constructed from the vertices illustrated in Figure 1.1. Three-point vertices are made from the intersection of three line segments at a point, and four-point vertices are made from the intersection of four line segments. External lines correspond to real particles which are observed in the final state and are on-shell. Internal lines correspond to virtual particles that are not observed in the final state and therefore may or may not be on-shell.

A diagram is tree-level if it uses the smallest number of vertices possible to depict an interaction having the correct initial and final states. For the case of two fermions,  $\phi(x_1), \phi(x_2)$ , which scatter via a gauge boson that subsequently decays to two possibly different fermions,  $\phi(x'_1), \phi(x'_2)$ , the three unique tree-level diagrams for a given configuration of  $\phi(x_1), \phi(x_2), \phi(x'_1), \phi(x'_2)$ , are illustrated in Figure 1.2.

These specific diagrams are depictions of the  $s, t, u$  channels respectively, named after the Mandelstam variables, which are Lorentz scalar combinations of incoming and outgoing momenta,

$$\begin{aligned} s &= -(k_1 + k_2)^2 = -(k'_1 + k'_2)^2 , \\ t &= -(k_1 + k'_1)^2 = -(k'_2 - k'_2)^2 , \\ u &= -(k_1 + k'_2)^2 = -(k_2 - k'_1)^2 . \end{aligned} \quad (1.37)$$

The Mandelstam variable  $s$  is the square of the momenta of the incoming particles in the center-of-mass (CM) frame and  $\sqrt{s}$  is the typical variable used by experimentalists to discuss the energy of colliding beams of particles.

Combining contributions from all valid Feynman diagrams according to the statistical rules appropriate for the particles which participate in the interaction, gives  $W(J)$  where

$$Z(J) = e^{iW(J)} \quad (1.38)$$

and the time ordered product of the fields can be found by taking the appropriate functional derivatives on  $W$ ,

$$\langle 0 | T\phi(x_1) \dots \phi(x_N) | 0 \rangle = \delta_1 \dots \delta_N iW(J)|_{J=0} . \quad (1.39)$$

### 1.3.3 Renormalization

Crucial for the LSZ formulation are two features of quantum fields, that they are fully separable in the infinite limit,  $\langle 0 | \phi(x) | 0 \rangle = 0$ , and that they are states of definite

**Figure 1.1:** The couplings for the SM gauge interactions.

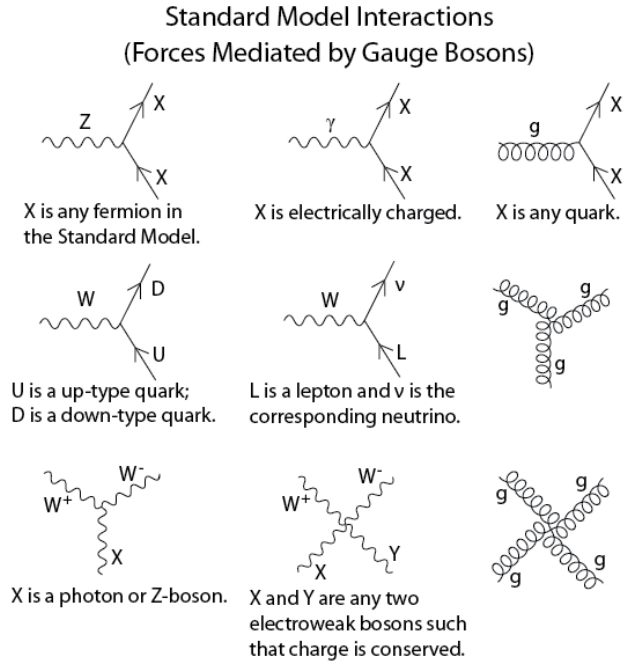
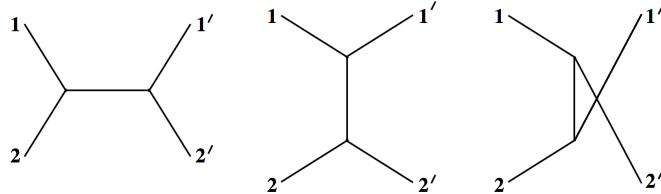


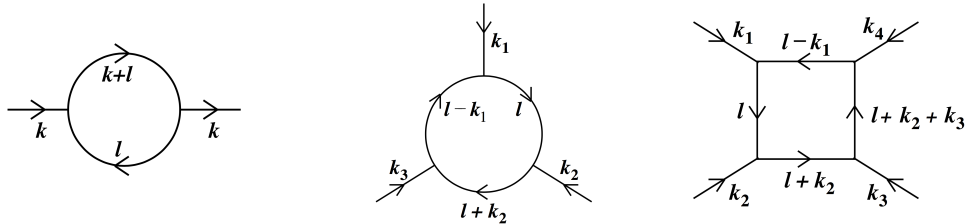
**Figure 1.2:** Below are Feynman diagrams for  $2 \rightarrow 2$  scattering. These are the tree-level diagrams of the  $s, t, u$  channels respectively.



momentum,  $\langle k|\phi(x)|0\rangle = e^{-ikx}$ . In the SM, which allows for fields to interact, these conditions are guaranteed by adjusting the strengths of the fundamental couplings,  $g_1, g_2, g_3$ . This ensures that the quantum states remain properly normalized, and is thus called renormalization.

Renormalization is necessary to account for corrections to the tree-level propagators

**Figure 1.3:** Renormalization takes place via a modification of the coupling parameters  $g_1, g_2, g_3$  to account for the contributions that loops of virtual particles make on the propagators and vertices. Below are diagrams keeping track of the flow of momentum for one-loop corrections to the propagator and three and four point vertices.



and vertices which arise from contributions of virtual particles connecting to form closed internal loops. The lowest order, one-loop, diagrams are illustrated in Figure 1.3. Renormalization is accomplished by introducing an energy scale, and assuming that the couplings are small compared to this scale. The coupling constants are therefore functions of energy and are quoted at a particular renormalization scale,  $\mu_R$ .

### 1.3.4 Cross sections and decay rates

The scattering amplitude  $\langle f|i \rangle$  is not a directly measurable observable. What can be observed is some finite distribution of data which may be analyzed to reveal information about the scattering amplitude. Quantum mechanics dictates that only predictions of probability are possible, and the final probability of observing a particular interaction is dependent on many variables, including the energies, types and angular momenta of the incoming and outgoing particles as well as the masses of the propagators and the orientation and efficiency of the detector.

A quantity typically measured is therefore the interaction cross section,  $\sigma$ , and

for the scattering of two incoming particles going to  $n'$  particles,  $2 \rightarrow n'$ , in the CM frame, the differential is

$$d\sigma = \frac{1}{4|\mathbf{k}_1|_{\text{CM}}} |\mathcal{T}|^2 d\text{LIPS}_{n'}(k_1 + k_2) \quad (1.40)$$

where the scattering matrix element,  $\mathcal{T}$ , is defined using Equation 1.33, as

$$\langle f | i \rangle = (2\pi)^4 \delta^4 \left( \sum k_{\text{in}} - \sum k_{\text{out}} \right) i \mathcal{T} \quad (1.41)$$

and the Lorentz-invariant measure of the phase space for the  $n'$  outgoing particles is

$$d\text{LIPS}_{n'}(k) = (2\pi)^4 \delta^4 \left( k - \sum_{j=1}^{n'} k'_j \right) \prod_{j=1}^{n'} dq'_j \quad (1.42)$$

with the Lorentz-invariant differential  $dq$ .

The cross section is used to calculate the rate at which a process occurs, but is not the only relevant factor in determining the overall production rate. The production rate of a given final state is also dependent on the incoming rate of possible interactions and is known as luminosity,  $\mathcal{L}$ . Luminosity has the units of inverse area per unit time and the total number of events produced is therefore proportional to  $\int \mathcal{L} dt$ . In any real detector, final state particles are collected only within a finite solid angle and the number of particles scattered into a given solid angle,  $\Omega$ , is given by

$$\frac{dN}{d\Omega} = \mathcal{L} \frac{d\sigma}{d\Omega} \quad . \quad (1.43)$$

It is also possible for particles to decay as  $1 \rightarrow n'$ . Massive particles decay to

lighter ones in both the fermion and boson sectors, with all massive bosons able to spontaneously decay via the diagrams in Figure 1.1. Of the charged fermions, only the first generation is stable for each type, and neutrinos are not known to spontaneously decay, but oscillate between flavors while propagating in free space. Like the differential cross section, the differential decay rate is a function of the scattering amplitude and has integration measure  $d\text{LIPS}$ ,

$$d\Gamma = \frac{1}{2E} |\mathcal{T}|^2 d\text{LIPS}_{n'}(k) . \quad (1.44)$$

The differential decay rate is inversely proportional to the energy of the particle,  $E = \sqrt{m^2 + p^2}$ . This means that comparatively heavy particles will decay faster than comparatively light ones and that energetic particles will appear to live longer for a stationary observer due to relativistic time dilation effects. The total decay rate of a given particle is found by summing the decay rates from each of the contributing processes, and the primary decay channels and rates for the fundamental particles are given in Table 1.4.

At CMS, the heaviest quark and the heaviest lepton both decay before reaching the detector volume. This makes  $b$  quarks the heaviest fundamental particles which can be seen to decay inside the detector, and therefore an object of interest. Additionally, their heavy mass means that they couple strongly with the Higgs boson which still has many properties that are under investigation. The  $W$  and  $Z$  bosons are both so massive that they decay before reaching the innermost layers of the detector and are often identified by their decay products pointing back to a common vertex.

**Table 1.4:** Below are listed the decay channels and rates for each of the unstable fundamental particles. At CMS, with the detection apparatus located a finite distance away from the interaction vertex, particles such as the  $W$ ,  $Z$  and Higgs bosons, as well as the  $t$  and tau, decay before reaching the first layer of the detector.

| Particle | Primary decay modes(s)                       | Total rest-frame $d\Gamma$ | Typical decay location |
|----------|--|----------------------------|------------------------|
| $W$      | $W \rightarrow \ell\nu$                      | X                          | Before reaching CMS    |
| $Z$      | $Z \rightarrow f\bar{f}$ (for $2M_f < M_Z$ ) | X                          | Before reaching CMS    |
| $\tau$   | $\tau \rightarrow W\nu_\tau$                 | X                          | Before reaching CMS    |
| $\mu$    | $\mu \rightarrow W\nu_\mu$                   | X                          | After leaving CMS      |
| $t$      | $t \rightarrow W^+b$                         | X                          | Before reaching CMS    |
| $b$      | $b \rightarrow W^-c$                         | X                          | Inside CMS             |
| $c$      | $c \rightarrow W^+s$                         | X                          | Inside CMS             |
| $s$      | $s \rightarrow W^-u$                         | X                          | Inside CMS             |

### 1.3.5 QCD and Proton Structure

The Feynman diagrams introduced in Section 1.3.2 describe the interactions between fundamental particles, but at the LHC, collisions take place between protons, which are composite.

One feature of the  $SU(3)$  symmetry of the strong force is that gluons carry one unit of color and one unit of anticolor while the quarks carry one unit of color charge. This is what allows gluons to interact with each other as well as with quarks. That quark confinement is necessitated by the  $SU(3)$  structure has not been conclusively determined, but observationally, a free gluon or quark has never been observed. Instead, quarks appear as bound in colorless (singlet) combinations called hadrons which are further classified as mesons ( $q\bar{q}$ ) or as baryons ( $qqq$  or  $\bar{q}q\bar{q}$ ), and are held together by gluons. Evidently, the binding energy of the quarks has a form such

that after a distance of roughly  $10^{-15}$  meters, the energy stored in the gluon field is greater than the energy needed to create a quark-antiquark pair, bringing the pair into existence. This process of energetic quarks creating particles as they separate is called hadronization and is an important effect at the LHC.

Protons are a type of baryon and at low energy, may combine with a single electron to form a neutral hydrogen atom. At higher energies, the internal structure of the proton becomes more evident, and it contains three valence quarks,  $uud$ , which are constantly exchanging gluons. When probed at high enough energy, or equivalently, at short enough length scales, these gluons can also each split into a  $q\bar{q}$  pair which typically reannihilate with each other. With gluons inside the proton splitting into quarks and coupling with other gluons, this forms a ‘sea’ of quarks and gluons, and as protons are accelerated to energies of GeV or TeV as is the case at the LHC, the fraction of the momentum of the proton attributed to the gluons becomes higher than that attributed to the valence quarks.

A proton-proton collider was therefore a sensible choice for the LHC. The physics goals of the project are to measure quantities associated with a wide range SM processes and to continue the search for evidence of new physics. Quarks interact with all of the SM gauge bosons as well as with the Higgs boson and the proton contains the lightest quarks of each type in addition to the gluons and sea. Colliding proton beams thus allow for the interactions between many different initial particle configurations to be explored, and with the exception of the neutrinos which interact only via the weak exchange of the  $Z$  boson and escape the detectors, all other fundamental SM particles have been directly observed at CERN.

## 1.4 Dark Matter

### 1.4.1 Experimental motivations

Albert Einstein's theory of general relativity, GR, has many experimental predictions which run counter to human intuition. GR predicts that massive objects warp a four-dimensional spacetime and thus feel mutual attraction. This has as a consequence, the prediction that even massless objects such as photons will experience a net deviation in their path near a massive object as a result of gravity and this effect was famously verified by Arthur Eddington through the observation of stars around the sun during a full solar eclipse. More recently, the direct detection of gravitational waves by the LIGO Collaboration also aligns with the GR predictions of distorted spacetime around colliding black holes. The time distortion effects due to the varying strengths of Earth's gravitational field on the surface and at the GPS satellites, provide precise tests of the quantitative predictions of GR. However, though these tests and others provide evidence that GR is an accurate theory of gravity, some basic predictions related to gravitational interactions do not agree with observations, motivating the concept for DM.

The first observational evidence for DM came from an analysis of the speeds of galaxies in the Coma cluster by Fritz Zwicky. The magnitude of the angular velocities of the galaxies was too great to be explained by the visible matter alone and DM is now believed to outweigh visible matter in a ratio of 5 : 1 throughout the universe and 10 : 1 throughout the Milky Way galaxy.

### 1.4.2 Simplified theoretical models

The defining features of DM are that it is massive and appears to interact on large scales only via the gravitational force. On the galactic and supergalactic scales, DM is distributed along similar structures as is visible matter, and it surrounds visible matter in extended halos.

Because DM has not yet been observed, the models of DM being considered in this thesis are simplified and based on minimal assumptions, the first being that DM is even capable of interacting with hadrons and is thus possible to produce at the LHC. While the visible sector of particles is diverse, the models used in this analysis consist of a single DM particle,  $\chi$ , which is assumed to be a fermion and may be different from  $\bar{\chi}$ .

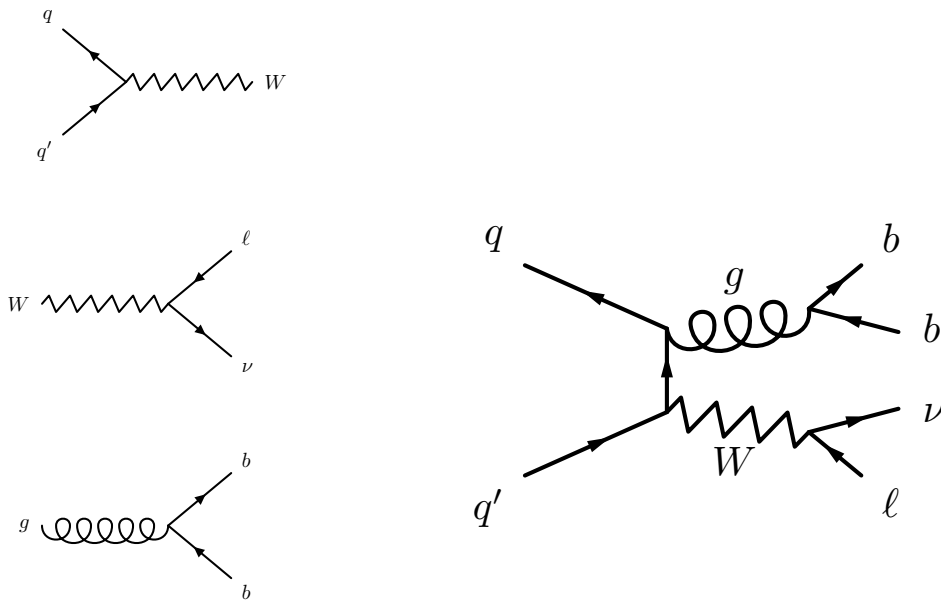
One way DM could couple to the SM is via the addition of a  $U(1)$  symmetry that gives rise to a vector gauge mediator,  $M$ . If some quarks are also charged under  $U(1)$ , then DM may be produced in the  $s$  channel as  $f\bar{f} \rightarrow M \rightarrow \chi\bar{\chi}$ . If  $M$  conserves parity in  $f\bar{f} \rightarrow M$ , it is said to have a vector coupling, and if it violates parity, it is termed axial-vector. In these models,  $M$  is assumed not to couple to leptons, but an effective field theory (EFT) model is also considered in this analysis which estimates a direct interaction between DM and photons. This coupling is mediated by a vertex  $\gamma\gamma\chi\bar{\chi}$  and allows for DM production via the channel  $pp \rightarrow \gamma \rightarrow \gamma\chi\bar{\chi}$ .

## 2 PHENOMENOLOGY OF PROCESSES

---

### 2.1 The Standard Model process $pp \rightarrow Wb\bar{b} \rightarrow \ell\nu b\bar{b}$

**Figure 2.1:** The Feynman diagram for the process  $pp \rightarrow Wb\bar{b} \rightarrow \ell\nu b\bar{b}$  is illustrated below, and is composed from the individual vertices illustrated on the left, each of which is described in Section 2.1.



#### 2.1.1 $pp \rightarrow W$

The  $W$  boson couples to all charged fermions and can be created during the collision of a quark-antiquark pair with a relative charge difference of  $e$ . In the proton are quarks and the most prevalent valence quark is the  $u$ . Therefore in a  $pp$  collision, the channel by which most  $W$  bosons are produced is via a the annihilation of a valence

$u$  quark from one proton with a  $\bar{d}$  from the sea of the other,  $u\bar{d} \rightarrow W^+$ . Quarks of higher generation can also be found inside the sea as the result of gluons splitting into  $q\bar{q}$  pairs, but all interactions are modified by a coefficient in the CKM matrix and higher generation mixing is thus suppressed. In this thesis, all modes of  $pp \rightarrow W^\pm$  production are considered.

### 2.1.2 $W \rightarrow \ell\nu$

Just as the  $W$  boson can be created by the collision  $q\bar{q}' \rightarrow W$ , it can also decay as  $W \rightarrow q\bar{q}'$ . This is known as hadronic  $W$  decay and can be a useful analysis channel for experimentalists, especially for decay products with energies approaching the TeV scale. Leptonic  $W$  decay,  $W \rightarrow \ell\nu$ , is also an important channel for experimentalists and is the one considered in this analysis. Because leptons constitute a negligible fraction of the sea, the detection of leptons at high energy after a  $pp$  collision is often a good indicator of the decay of a massive gauge boson,  $W \rightarrow \ell\nu$  or  $Z \rightarrow \ell\bar{\ell}$ .

The  $W$  boson is much heavier than any of the leptons and therefore decays with roughly equal probability to any of  $e\nu_e, \mu\nu_\mu, \tau\nu_\tau$ . From Table 1.4, tauons created at CMS subsequently decay before reaching the detector, so for this analysis, the decay channel of the  $W$  investigated is  $W \rightarrow \ell\nu$  where  $\ell \in e, \mu$ .

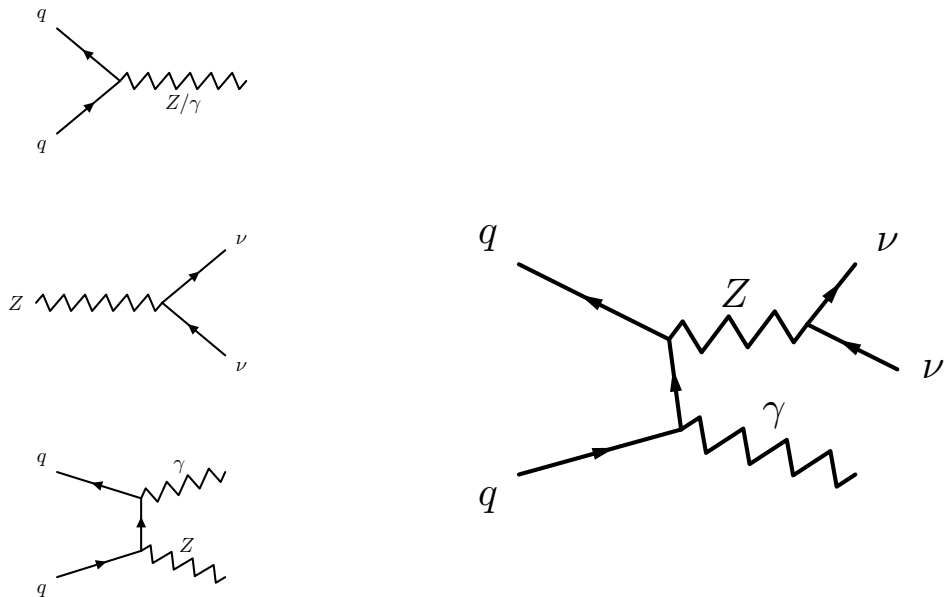
### 2.1.3 $g \rightarrow b\bar{b}$

Because quarks couple strongly to gluons and  $q\bar{q}' \rightarrow W$  has been shown to be an important production channel in  $pp$  collisions, it is possible for one of the initial state quarks to radiate a gluon. This is called initial state radiation, ISR, and if the gluon

is produced with enough energy, it is capable of splitting to a quark-antiquark pair. In particular, a  $g \rightarrow b\bar{b}$  vertex can be added to either of the incoming quarks to form  $pp \rightarrow Wb\bar{b} \rightarrow \ell\nu b\bar{b}$ .

## 2.2 The Standard Model process $pp \rightarrow Z\gamma \rightarrow \nu\bar{\nu}\gamma$

**Figure 2.2:** The Feynman diagram for the process  $pp \rightarrow Z\gamma \rightarrow \nu\bar{\nu}\gamma$  is illustrated below, and is composed from the diagrams illustrated on the left, each of which is described in Section 2.2.



### 2.2.1 $pp \rightarrow Z/\gamma$

Similar to the  $W$  boson, the  $Z$  boson and the photon can also each be produced via the collision of quarks in the process  $q\bar{q} \rightarrow Z/\gamma$ . Unlike interactions with the  $W$

boson, interactions with  $Z/\gamma$  conserve parity invariance and do not transport charge. Any interaction which can happen as mediated by a photon can also happen with the exchange of a  $Z$  boson, but for collisions at  $\sqrt{s} < M_Z = 90$  GeV, the  $Z$  can not be made on-shell. In this low energy regime  $\gamma$  exchange dominates, but in 2015, the LHC ran at  $\sqrt{s} = 13$  TeV and the relative mass difference between the  $Z$  and the  $\gamma$  played a negligible role in their relative rates of production.

### 2.2.2 $Z \rightarrow \nu\bar{\nu}$

The only particle which the  $Z$  boson can couple to but the photon can not is the neutrino. At  $\sqrt{s} = 13$  TeV, the mass differences between the five lightest flavor of quark and the six leptons are negligible and the  $Z$  boson can decay into any kinematically allowed pairs,  $Z \rightarrow f\bar{f}$ . Including the three color possibilities for each quark, these are  $3 \times 5 + 6 = 21$  final states, each of which has roughly the same branching fraction. Therefore only approximately  $2/7$  of  $Z$  decays happen in the leptonic channel  $Z \rightarrow \ell\bar{\ell}$ . and of these decays, approximately  $2/3$  happen as  $Z \rightarrow \nu\bar{\nu}$ .

### 2.2.3 $pp \rightarrow Z\gamma$

With the photon coupling only to electrically charged particles, the only place where a vertex containing a photon could be attached to either of the upper two left diagrams in Figure 2.2 is on one of the quarks. Photons are massless and therefore stable and so are a final state observable. Like the gluon in  $pp \rightarrow Wb\bar{b} \rightarrow \ell\nu b\bar{b}$ , the photon is an example of ISR. In the CM frame of the colliding  $q\bar{q}$ , which is approximately the lab rest frame for colliding beams of equal energy as is the case at the LHC, conservation

of momentum dictates that the  $Z$  boson and photon should have equal and opposite momenta.

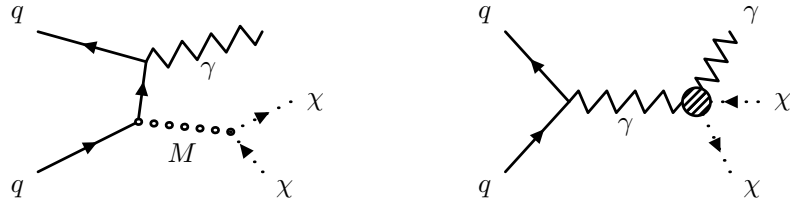
Unlike any of the other fermions, neutrinos are electrically neutral and therefore only interact via the weak force. So while the cross sections for most fermion-fermion interactions involve contributions from the comparatively stronger electromagnetic and strong forces, the neutrino cross section contains contributions from only the  $W$  and  $Z$  bosons at tree-level and is much smaller than that of the charged fermions. This makes the detection of neutrinos very difficult in general, and impossible to do with present technology given the extreme backgrounds present in a collider setting.

In the case where the ISR photon is recoiling against a  $Z$  boson which decays to neutrinos, no direct detection of the  $Z$  boson or of its decay products is possible, leaving only the photon visible in the final state. This is called the monophoton signature, where a photon is observed recoiling against apparently nothing, and while the monophoton signature is predicted to be observed as a result of SM process as in  $pp \rightarrow Z\gamma \rightarrow \nu\bar{\nu}\gamma$ , if the observed monophoton cross section is measured to be higher than predicted, it could also be an indicator of physics beyond the SM (BSM). Specifically, the monophoton signature used in searches for dark matter.

### **2.3 $pp \rightarrow \gamma + \text{invisible}$**

The existence of particle dark matter is well motivated, and the simplified model theories of DM used in this thesis allow for interactions which can result in the monophoton signature. One of the classes of models considered is a  $U(1)$  gauge theory

**Figure 2.3:** Feynman diagrams for the DM process  $pp \rightarrow \gamma + \text{invisible}$  using simplified models are illustrated below. On the left is the  $U(1)$  gauge model in which DM production is mediated by  $M$  which can be either vector or axial-vector. On the right is the diagram for DM production using an EFT model of the  $\gamma\gamma\chi\bar{\chi}$  coupling.



in which  $\chi\bar{\chi}$  is produced via a vector or axial-vector mediator  $M$  which couples to quarks. The tree-level process in this model which leaves a monophoton signature is illustrated on the left of Figure 2.3, and the relevant parameters governing the cross section of this interaction are the masses of the two particles,  $m_\chi$  and  $m_M$ , and the strengths of the couplings between  $M$  and quarks,  $g_{Mq}$ , and between  $M$  and DM,  $g_{m\chi}$ . An EFT describing the four-point interaction vertex  $\gamma\gamma\chi\bar{\chi}$  is also considered and illustrated on the right side of Figure 2.3. In this theory, the coupling is a function of two parameters,  $k_1$  and  $k_2$ , and is moderated by a mass scale,  $\Lambda$ . The other parameter in the EFT is  $m_\chi$ , and by measuring the cross section for  $pp \rightarrow \gamma + \text{invisible}$  in comparison with the SM prediction, estimations or limits can be set on the parameters used in either of these two models.

## 3 THE LHC AND CMS

---

The measurements presented in this thesis are performed on data of proton-proton collisions collected by the Compact Muon Solenoid (CMS) detector and provided by the Large Hadron Collider (LHC) at the European Center for Nuclear Research (CERN). The LHC was designed to probe physics at the scale of TeV and is capable of operating at multiple energy scales. As measured in the CM frame of protons colliding inside CMS, the LHC operated at  $\sqrt{s} = 8$  TeV in 2012 and  $\sqrt{s} = 13$  TeV in 2015. The measurement of the  $pp \rightarrow Wb\bar{b}$  cross section is performed using 19.8  $\text{fb}^{-1}$  of integrated luminosity collected at  $\sqrt{s} = 8$  TeV and the measurement of the  $pp \rightarrow Z\gamma \rightarrow \nu\bar{\nu}\gamma$  cross section and the extensions to set limits on DM models uses 2.3  $\text{fb}^{-1}$  of data collected at  $\sqrt{s} = 13$  TeV.

### 3.1 The Large Hadron Collider

The LHC is a single-ring, double-bore particle accelerator and collider located on the border of France and Switzerland outside Geneva. It was built using the existing 26.7 km of tunnels from the Large Electron Positron collider and hosts four primary experiments, located at four interaction points where beams of hadrons are made to cross. Of the four experiments, two (CMS and ATLAS) are built for studying SM processes and searching for new physics in general, one (ALICE) is designed to investigate quark-gluon plasma resulting from the high energy collisions of heavy ions such as lead, and one (LHCb) was built for the study of b-mesons and CP violation.

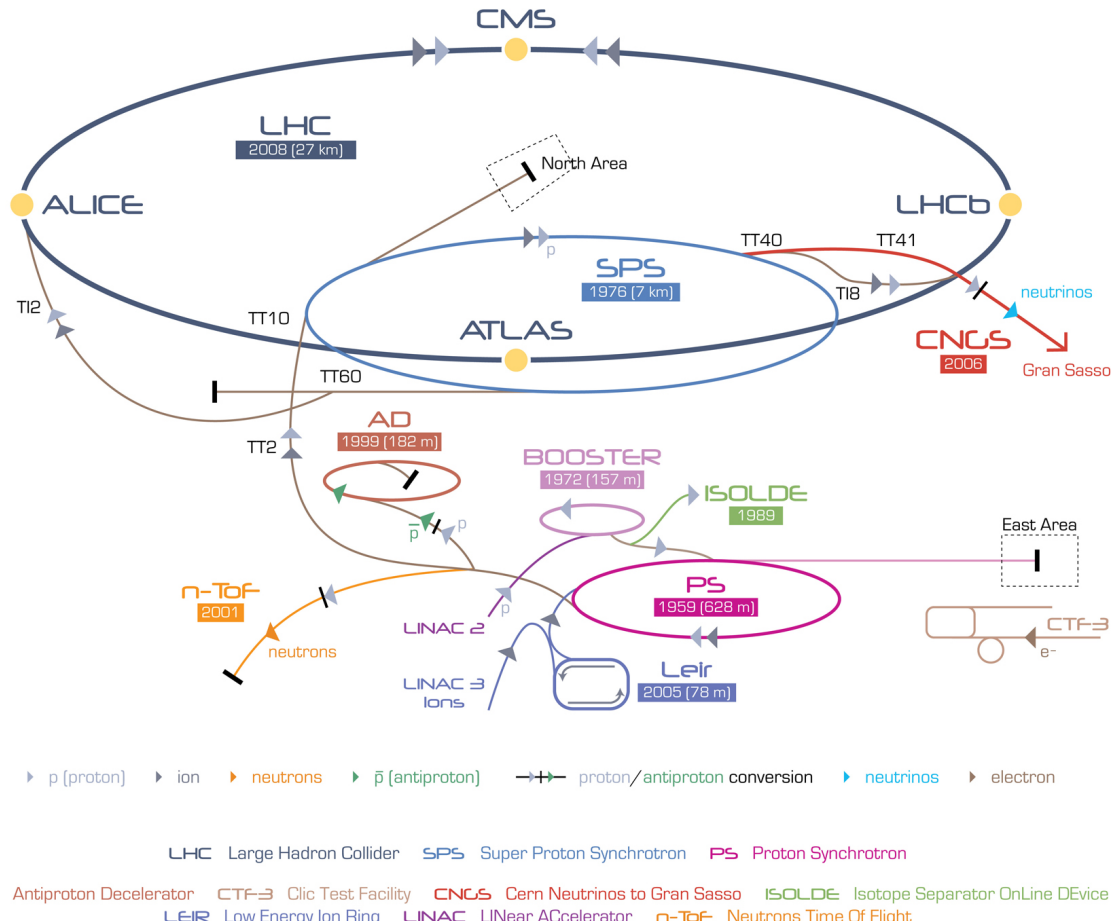
### 3.1.1 LHC pre-acceleration

To accelerate protons to their collision energy, a multi-stage procedure is used and the major components of the accelerator infrastructure are illustrated in Figure 3.1. First, protons are separated from electrons in neutral hydrogen gas before entering the linear accelerator (LINAC2) which brings them up to an energy of 50 MeV using a series of oscillating electric potentials. In this process, rather than having a continuous stream of accelerating protons, the protons are grouped into bunches, and the beam retains this structure of distinct groups of protons separated by gaps throughout the acceleration procedure. After the LINAC2, protons enter the Proton Synchrotron Booster (BOOSTER) where they are accelerated to 1.4 GeV and prepared for injection into the Proton Synchrotron (PS). Inside the PS, bunches are accelerated to 26 GeV before being injected into the Super Proton Synchrotron (SPS) where they are further accelerated to 450 GeV. After the SPS, bunches of protons are sent into the LHC.

### 3.1.2 LHC acceleration

The work of accelerating and containing the protons which form the beam of the LHC is done by superconducting magnets. They are cooled to a temperature of 1.9 K using liquid helium and are housed in the LHC dipole apparatus diagrammed in Figure 3.2. The dipole contains two beam pipes which are each surrounded by superconducting coils of Niobium Titanium (NbTi) which carry oscillating currents when in operation. These constitute RF cavities operating at 400 MHz and having the ability to circulate proton bunches in opposing directions between the two beam pipes with a spacing of 25 ns between bunches. The magnets are capable of reaching a strength of over 8 T,

**Figure 3.1:** Before protons are released into the LHC for final acceleration and collision, they pass through the LINAC2, BOOSTER, PS, and SPS, undergoing acceleration at each stage.



a constraint imposed by the desired energy scale of the accelerator and the radius of the existing LEP tunnels in which the LHC was built.

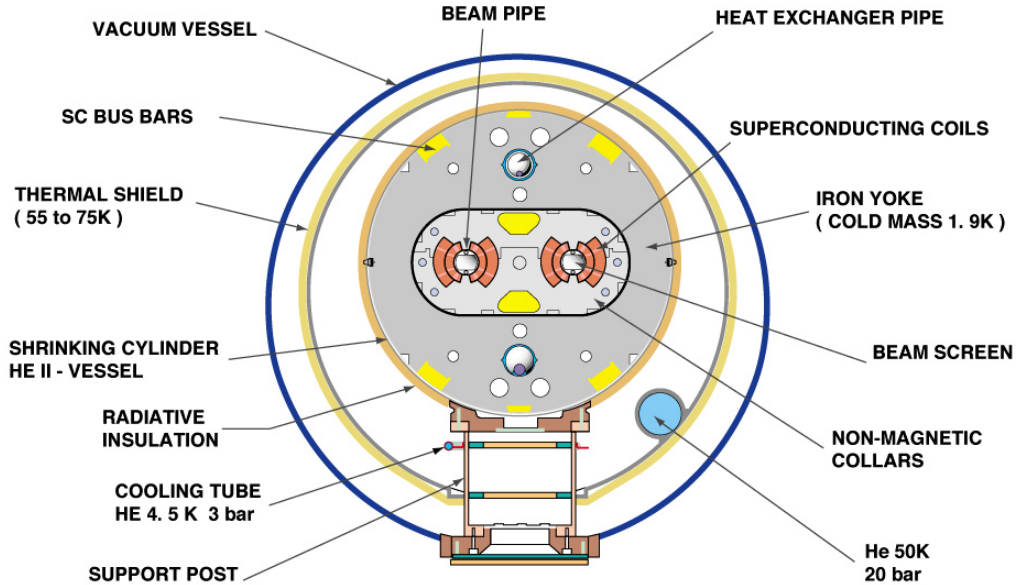
The Lorentz-invariant magnetic force on a particle of charge  $q$ , moving at velocity  $\mathbf{v}$  in a magnetic field  $\mathbf{B}$  is

$$\mathbf{B} = q\mathbf{v} \times \mathbf{B} \quad (3.1)$$

**Figure 3.2:** Below is a cross section of the LHC dipole apparatus. It contains two beam pipes, each surrounded by superconducting magnetic coils which are held in place by an iron yoke. The system is cooled to a temperature of 1.9 K and is thermally isolated as well as protected from radiation.

### CROSS SECTION OF LHC DIPOLE

---



CERN AC \_HE107A\_ V02/02/98

and the relativistic version of Newton's second law states

$$\mathbf{F} = \frac{d\mathbf{p}}{dt} = \frac{d}{dt} (\gamma m_0 \mathbf{v}) \quad (3.2)$$

where  $\gamma$  is the relativistic correction factor and  $m_0$  is the rest mass of the particle. These can be solved to find that the magnetic field required to hold a proton in planar

circular motion as in the LHC is

$$\mathbf{B} = \frac{\mathbf{p}}{qR} \quad (3.3)$$

where  $R = 4.3$  km. [todo - unit conversion]

The rate at which a particular collision process occurs at the LHC is proportional to the cross section of that interaction and the luminosity of the colliding beams as given in Equation 1.43. Assuming a Gaussian beam distribution, the machine parameters determine  $\mathcal{L}$  as

$$\mathcal{L} = \frac{N_b^2 n_b f_{\text{rev}} \gamma_r}{4\pi \epsilon_n \beta_*} \mathcal{F}(\theta) \quad (3.4)$$

where  $N_b$  is the number of particles per bunch,  $n_b$  is the number of bunches per beam,  $f_{\text{rev}}$  is the revolution frequency of the bunches,  $\gamma_r = E_p/m_p$  is the relativistic gamma factor for protons at energy  $E_p$ ,  $\epsilon_n$  is the normalized emittance which characterizes bunch width,  $\beta_*$  is a measure of the betatron oscillation envelope, and  $\mathcal{F}(\theta)$  is a relativistic geometrical correction factor which is a function of the angle at which the beams cross. In addition to pushing the energy frontier, the LHC also has a significantly greater  $\mathcal{L}$  than previous hadron colliders. [Reference to Tevatron]

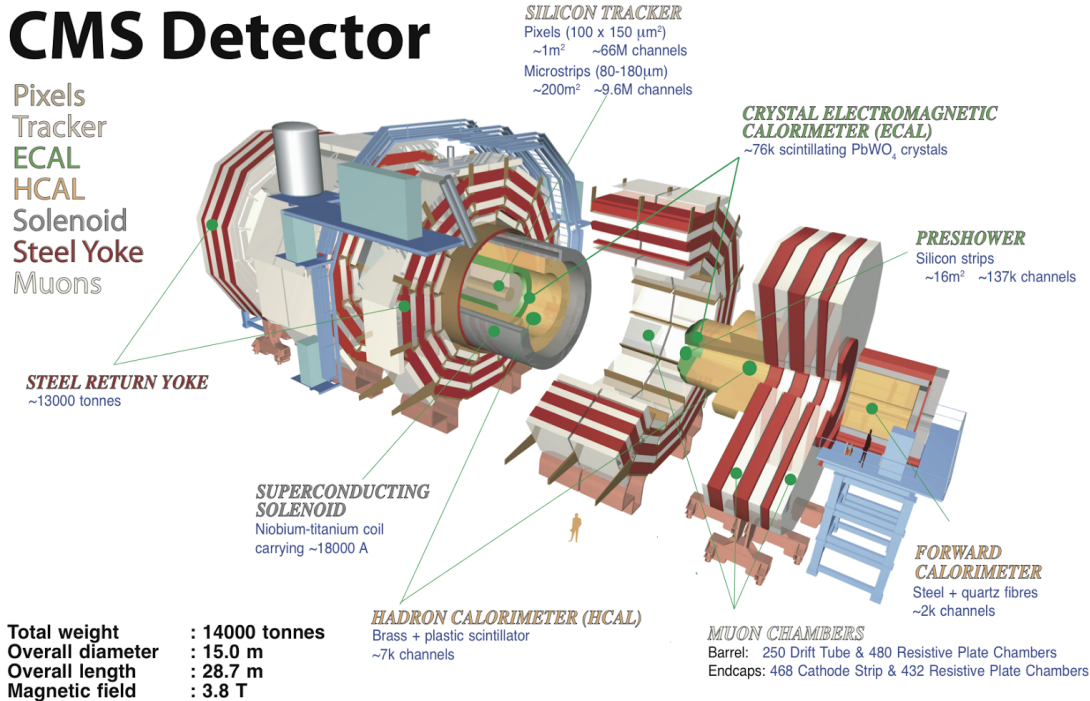
## 3.2 The Compact Muon Solenoid Detector

The CMS detector was built at Interaction Point 5 on the LHC ring to collect particle collision data exploiting the full physics reach of the LHC. The analysis of these data includes the discovery of the Higgs boson[REF] and high precision measurements of SM processes, as well as searches for physics beyond the standard model. To be

able to perform such precision measurements, CMS was designed with four main subdetectors that work in concert and with a superconducting solenoid. The tracking and most of the calorimetric detectors are inside the solenoid while the muon detectors are outside. When running, the solenoid produces a 3.8 T uniform magnetic field in its interior, and has a uniform 2 T field over the bulk of the detector external to the solenoid.

The innermost of the subdetectors is the tracker which uses silicon pixel and strip detectors to record the tracks of charged particles passing through it. The tracks are used in conjunction with the 3.8 T magnetic field to measure the momentum of these particles and this information is used for identifying the primary interaction vertex as well as locating secondary vertices from the decay of heavy flavor quarks such as the b or c. Outside the tracker is the electromagnetic calorimeter (ECAL), which is designed to have good energy resolution in recording the electromagnetic interactions of charged particles such as electrons or photons over a wide range of angles. The hadronic calorimeter (HCAL) is outside the ECAL and is designed to absorb energy which comes in the form of neutral hadrons and provide good resolution in missing transverse energy,  $E_T^{\text{miss}}$ . Outside the calorimeters is the solenoid and steel return yolk, and the outermost layers of the detector are dedicated to the efficient detection of muons. The overall length of CMS is 21.6 m, with a radius of 7.3 m and a total weight of 12500 tons.

**Figure 3.3:** The CMS detector consists primarily of a tracker and electromagnetic and hadronic calorimeters which are mostly located inside a 3.8 T field provided by a superconducting solenoid, as well as a muon detection system located outside the solenoid.



### 3.2.1 Geometry

The coordinate system used by CMS is one in which the z-axis is aligned with the beam pipe, the y-axis is pointing upward vertically and the x-axis points radially inward toward the center of the LHC ring. The detector itself is mostly cylindrically symmetric about the beam pipe so cylindrical coordinates are also used. In this system,  $r$  is the radial distance as measured from the beam pipe, the azimuthal angle,

$\phi$ , is measured up from the x-axis in the x-y plane, and the polar angle,  $\theta$ , is measured down from the z-axis. The angle  $\theta$  is commonly replaced by pseudorapidity,

$$\eta = -\ln(\tan \theta/2) \quad (3.5)$$

since the distribution of particles is roughly constant as a function of  $\eta$ . For the calorimeters, “barrel” refers to the region of  $|\eta| < 1.4442$ , and “endcap” to the region  $3.0 > |\eta| > 1.566$ . Instrumentation cables are run through the gap between the barrel and endcap, so this area has detecting components. The HCAL forward region covers  $3.0 < |\eta| < 5$  and the tracker extends to  $|\eta| < 2.5$ .

### 3.2.2 Magnet

To precisely measure the momentum of a charged particle, it is necessary to measure radius of curvature of that particle as it moves through a magnetic field. The momentum resolution varies as

$$\frac{\delta p}{p} \sim \frac{1}{L^2 B} \quad (3.6)$$

where  $L$  is the length of the track of the particle through a magnetic field of strength  $B$ . For particles at high energy, this requires a very strong magnetic field which is achieved by the superconducting solenoid in CMS. The solenoid operates at 3.8 T with a bore of 3 m in radius and 12.5 m in length and is constructed from four layers of NbTi superconductor. The steel yoke which provides physical support for the CMS structure and serves as an absorber for the muon system is fully saturated by the

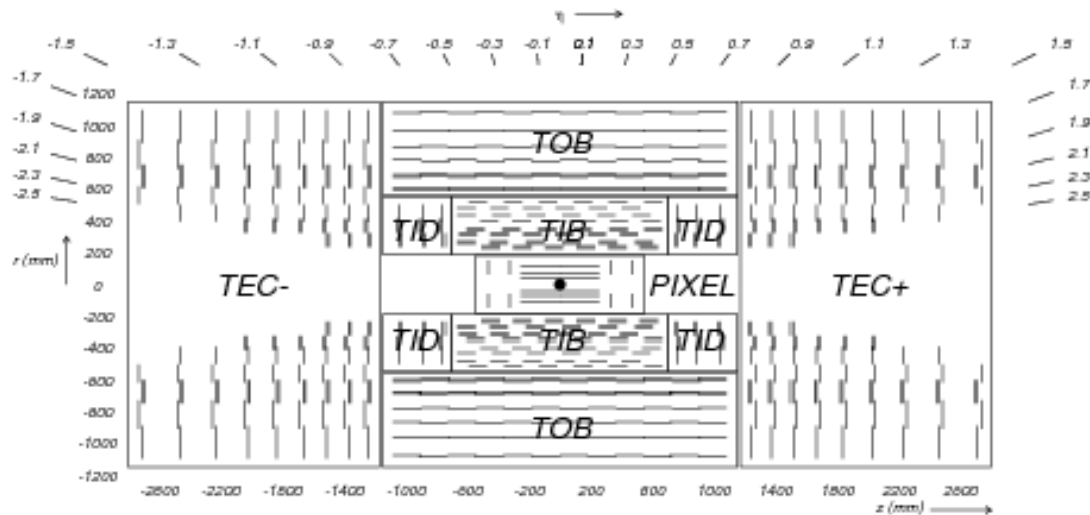
fringe magnetic field from the solenoid.

### 3.2.3 Tracking System

The inner tracking system of CMS is designed to provide precise and efficient measurements of the trajectories of charged particles produced during collisions, as well as a precise reconstruction of secondary vertices. The tracker has a length of 5.8 m and a radius of 1.25 m in a cylindrical structure surrounding the interaction point, as illustrated in Figure 3.4.

At the core of the tracker and closest to the beam line are three concentric cylindrical layers of hybrid pixel detector modules which are complemented by two discs of pixel modules on each end and extend a to a distance of 10 cm from the beam line. [TODO - Explain - silicon] In total, the pixel component of the tracker covers an area of about  $1 \text{ m}^2$  with 66 million pixels. External to the pixel detector are the tracker inner barrel and discs (TIB/TID) which are made from silicon strips and extend out to a distance of 55 cm. There are four layers of strips in the TIB, with 3 discs at each end. The tracker outer barrel (TOB) is composed of 6 layers of micro-strip sensors and extends in z between  $\pm 118 \text{ cm}$  and to a radius of 116 cm. At the end of the z range for the TOB are the tracker end caps (TEC) which cover the ranges  $124 < |z| < 282 \text{ cm}$  and  $22.5 \text{ cm} < r < 113.5 \text{ cm}$ . Each TEC is composed of 9 discs, each carrying up to 7 rings of silicon micro-strip detectors. In total, the tracker contains 9.3 million strips which cover an area of  $198 \text{ m}^2$  and extends to an acceptance of  $|\eta| < 2.5$ . For tracks with momentum on the order of 100 GeV, the momentum resolution is around 1-2% up to  $|\eta| < 1.6$  and degrades to around 10%

**Figure 3.4:** Below is a schematic of the CMS tracking system where each line represents a detector module. The system is made from silicon pixels and silicon microstrips distributed into four sections, TIB, TID, TOB, TEC.



with increasing  $\eta$ .

### 3.2.4 Electronic Calorimeter

The electronic calorimeter (ECAL) is a homogeneous calorimeter made from nearly 76000 crystals of lead tungstate ( $\text{PbWO}_4$ ) mounted in the barrel and endcap sections with a preshower detector located in front of the endcaps, arranged as shown in Figure 3.5 In the barrel, avalanche photodiodes are used as photodetectors, and in the endcap vacuum phototriodes are used. The material  $\text{PbWO}_4$  was chosen for its properties of being dense, optically transparent and radiation hard. The radiation length inside the ECAL is typically less than 1 cm with a Moliere radius of 2.2 cm

and about 80% of the light is emitted from a crystal within the first 25 ns. Since the length of a given crystal is on the order of 20 cm, most photons and electrons deposit all of their energy within the ECAL, and do not reach the HCAL.

The use of PbWO<sub>4</sub> crystals allows for excellent position and timing resolution with the energy resolution given by

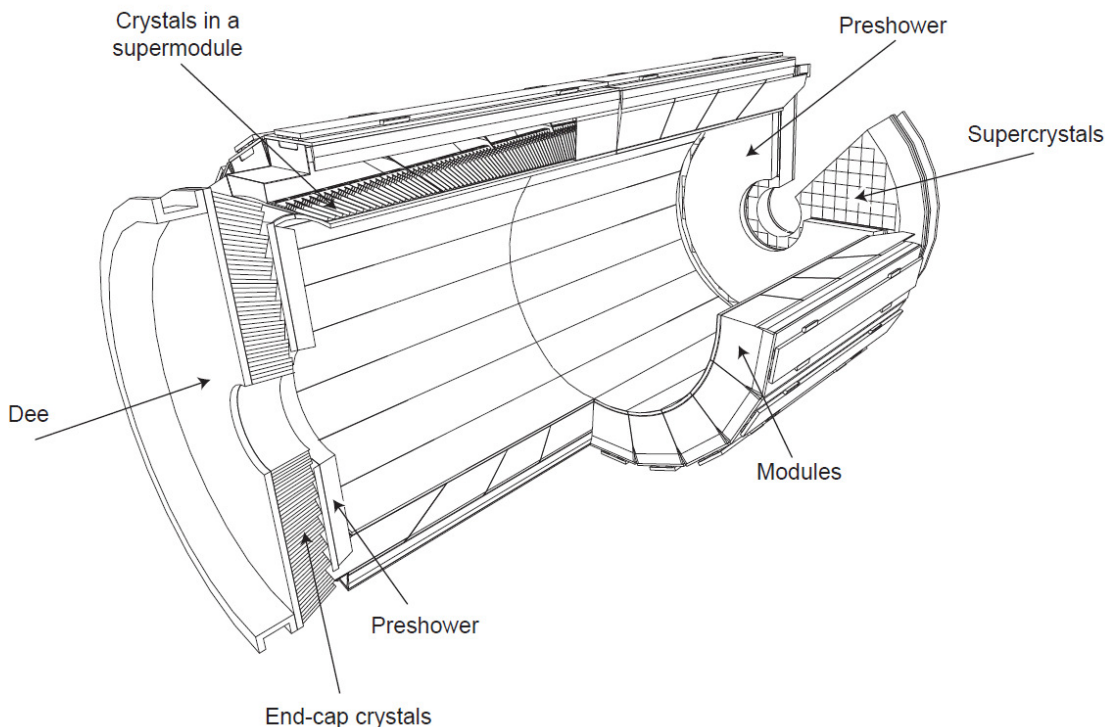
$$\left(\frac{\delta_E}{E}\right) = \left(\frac{2.8\%}{\sqrt{E}}\right)^2 + \left(\frac{0.12}{E}\right) + (0.30\%)^2. \quad (3.7)$$

In this expression, the first term comes from the statistical error in the measurement which arises from the stochastic nature of electromagnetic shower evolution and the second term represents the error in the measurement which results from noise in the electronics or energy deposits from additional soft interactions. The ECAL provides stable and accurate measurements of energies over a range from 1 GeV to 1 TeV, with the upper limit set by the energy at which electromagnetic showers penetrate through the ECAL into the HCAL. [REF][TODO - how much?] With time, after undergoing a heavy bombardment of high energy radiation, the PbWO<sub>4</sub> crystals physically deteriorate and develop nonuniform light transmission properties. [REF] This is monitored and corrected for using a laser calibration system that probes for changes in crystal transparency.

### 3.2.5 Hadronic Calorimeter

Situated mostly between the ECAL and the superconducting solenoid is the hadronic calorimeter (HCAL) which plays a crucial role in the measurement of hadron jets and particles such as neutrinos which escape the detector and result in apparent missing

**Figure 3.5:** Below is a diagram of the ECAL, which sits between the tracker and HCAL in CMS. It is made from PbWO<sub>4</sub> crystals throughout the volume with avalanche photodiodes in the barrel and vacuum phototriodes in the endcaps.



transverse energy. The HCAL is designed to contain the energy of neutral particles which pass through the ECAL and is therefore made from dense materials such as steel and brass interleaved with scintillating material. Because the HCAL is designed to fit between these two components, it takes the shape of a hollow cylinder of inner radius 1.77 m and outer radius 2.95 m and one half of the HCAL is illustrated in Figure 3.6.

The barrel of the HCAL (HB) extends to  $|\eta| < 1.3$  and is constructed from brass absorber plate wedges aligned parallel to the beam axis and mounted in an overlapping configuration, with a smaller amount of steel used in the inner and outermost wedges for structural stability. The endcap of the HCAL (HE) extends this coverage to  $|\eta| < 3.0$  and is complemented by the forward hadron calorimeter (HF) which is made from the comparatively radiation-hard steel plates embedded with quartz fibers. Inside the barrel region there is an additional layer of the HCAL, the outer calorimeter (HO), which is located just outside the solenoid and uses it as an absorber for energetic showers which start late in the HB.

In the HB, HO and HE, light from particle showers [TODO - not exactly ..] inside scintillators and collected by quartz fibers and then used as an estimate of the total energy of the shower. In the HF, this estimate is made using the Cherenkov radiation from particles with energy above 190 keV collected by the quartz fibers. For the two cases, the energy resolution takes the same functional form

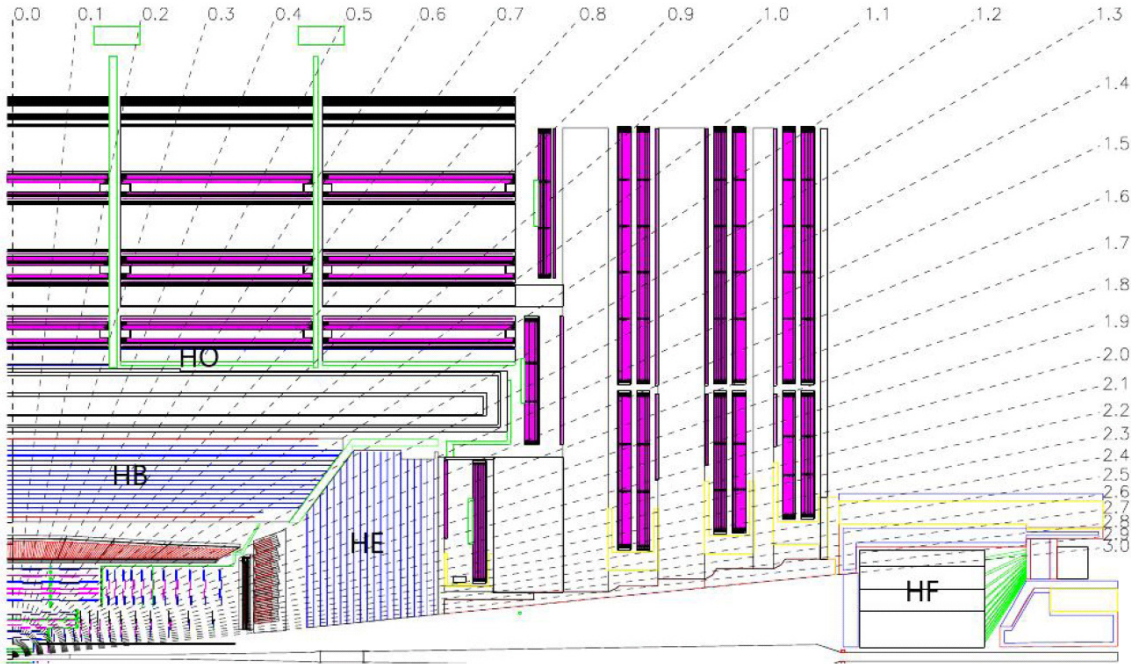
$$\left( \frac{\delta_E}{E} \right) = \left( \frac{A}{\sqrt{E}} \right)^2 + (B)^2 \quad (3.8)$$

where  $A$  is 90% (172%) in the HB/HO/HE (HF) and relates to the stochastic uncertainty of shower evolution and  $B$  is 4.5% (9.0%) and comes from uncertainties in calibration.

### 3.2.6 Muon System

Muons play a central role in the physics program outlined by CMS and the muon detection system is positioned as the outermost layer of the detector. Unlike the other

**Figure 3.6:** A schematic layout of the HCAL, which complements the ECAL in providing a measurement of the total energy produced in a collision. The HCAL is made from brass and steel plates, embedded with quartz fibers.



charged leptons, muons typically pass through the ECAL and HCAL and deposit only a fraction of their energy, so a dedicated muon system is necessary in order to determine the momentum of these particles. The muon system is composed of three different kinds of gaseous detectors, drift tubes (DTs), resistive plate chambers (RPCs) and cathode strip chambers (CSCs) and their layout is illustrated in Figure 3.7.

The barrel region of the muon system is covered by DTs in the range  $|\eta| < 1.2$

and the endcaps are covered by CSCs in the range  $0.9 < |\eta| < 2.4$ . The RPCs are located in the range  $|\eta| < 1.6$  and provide fast, independent and highly segmented transverse momentum measurements of muons.

The DT system is composed of 4 stations which form concentric cylinders about the beam line and contain 172000 sensitive wires. As charged particles enter the DTs, they ionize the Ar/CO<sub>2</sub> gas mixture, knocking off electrons which then are attracted to the positively charged wires.

The CSCs are less sensitive to uneven magnetic fields and high particle rates so are therefore used in the endcaps. They are made from crossed arrays of positively charged wires and negatively charged strips in gas and are composed of six layers, giving them precise timing as well as positional information. As an upgrade between the 2012 and 2015 data taking periods, a fourth layer of CSCs was added to the CMS detector, adding to the three which were present in 2012.

The RPCs are built from two sheets held at opposite charges and separated by a gas volume. As muons move through the chamber, electrons are ionized from the gas and attracted to small metallic strips which they reach after a small but well known time delay. The timing resolution of RPCs is on the order of 1 ns.

**Figure 3.7:** The CMS muon system uses DTs, RPCs, and CSCs to provide muon detection up to  $\eta < 2.4$ . Shown below is the geometrical arrangement of the different muon subsystems and how they fit with the rest of the CMS detector.

